

LENSING AND THE WARM HOT INTERGALACTIC MEDIUM.

F. ATRIO-BARANDELA¹, J. P. MÜCKET²*Draft version September 28, 2021*

ABSTRACT

The correlation of weak lensing and Cosmic Microwave Anisotropy (CMB) data traces the pressure distribution of the hot, ionized gas and the underlying matter density field. The measured correlation is dominated by baryons residing in halos. Detecting the contribution from unbound gas by measuring the residual cross-correlation after masking all known halos requires a theoretical understanding of this correlation and its dependence with model parameters. Our model assumes that the gas in filaments is well described by a log-normal probability distribution function, with temperatures $10^5\text{--}10^7\text{K}$ and overdensities $\xi \leq 100$. The lensing-comptonization cross-correlation is dominated by gas with overdensities in the range $\xi \approx [3 - 33]$; the signal is generated at redshifts $z \leq 1$. If only 10% of the measured cross-correlation is due to unbound gas, then the most recent measurements set an upper limit of $\bar{T}_e \lesssim 10^6\text{K}$ on the mean temperature of Inter Galactic Medium. The amplitude is proportional to the baryon fraction stored in filaments. The lensing-comptonization power spectrum peaks at a different scale than the gas in halos making it possible to distinguish both contributions. To trace the distribution of the low density and low temperature plasma on cosmological scales, the effect of halos will have to be subtracted from the data, requiring observations with larger signal-to-noise ratio than currently available.

Subject headings: cosmic background radiation - cosmology: observations - cosmology: theory - intergalactic medium - gravitational lensing: weak

1. INTRODUCTION.

A recent account of the baryon distribution in the local Universe concluded that about half the baryons synthesized in the Big-Bang have yet to be identified (Shull, Smith & Danforth 2012) confirming an earlier deficit of baryons found by Fukugita, Hogan & Peebles (1998). Numerical simulations (Cen & Ostriker 1999; Davé et al 1999, 2001, Cen & Ostriker 2006, Smith et al 2011) indicated that only 10-20% of all baryons are in collapsed objects. Baryons in Intergalactic Medium (IGM) exist in a wide range of densities and temperatures. Penton, Stocke & Shull (2004) and Lehner et al (2007) concluded that another $\sim 30\%$ resides in low redshift Ly α absorption systems, while the rest could reside in the shock-heated IGM with temperatures $10^5\text{--}10^7\text{K}$ and overdensities $\xi \leq 100$. This unbound gas is usually known as Warm-Hot Intergalactic Medium (WHIM). Identification of the WHIM phase and its spatial distribution at low redshift is an on-going theoretical and observational effort (for a review, see McQuinn 2016). The low density makes it difficult to detect the WHIM in emission (Soltan 2006); more promising is using absorption lines in the far ultraviolet to the soft X-ray range but some earlier detections remain controversial (Shull et al 2012). Cappelluti et al (2012) and Roncarelli et al (2012) have searched for the contribution of the WHIM to the diffuse X-ray emission but failed to find a statistically significant result.

Since the WHIM is highly ionized, there has been an extensive search on the thermal and kinematic Sunyaev-Zel'dovich CMB temperature anisotropies (hereafter tSZ and kSZ, Sunyaev & Zeldovich 1970; Sunyaev & Zeldovich 1972) generated by this baryon component (Atrio-Barandela & Mücke 2006; Atrio-Barandela et al 2008). Cross-correlation of CMB temperature data from *WMAP* or *Planck* with matter templates produced only marginal evidence of tSZ anisotropies due to the WHIM (Suarez-Velázquez et al 2013b, Génova-Santos et al 2013, Génova-Santos et al 2015). Combining X-ray and tSZ observations could be a promising tool to study the WHIM (Ursino, Galeazzi & Hufferberger 2014). The first evidence of warm-hot gas beyond the virial radius of clusters was presented in Planck Collaboration (2013) who detected a filamentary structure between the cluster pair A399-A401. The distribution of gas in a cosmic web has also been confirmed by XMM-Newton observations of the cluster Abell 2744 by Eckert et al (2015) who found filamentary structures of gas at temperature 10^7K and coherent over a scale of 8Mpc. At those temperatures and densities, the kSZ effect can have a contribution of similar amplitude to the tSZ effect. The kSZ effect has been used to trace large scale peculiar velocity fields (Kashlinsky et al 2008, Atrio-Barandela et al 2015) and the anisotropies due to the pair-wise velocity dispersion of clusters and galaxies have been measured (Hand et al 2012, Soergel et al 2016, Schaan et al 2016, de Bernardis et al 2017). These latter observations probe baryons on cluster and galaxy scales but have not yet provide a measurement of the fraction of free electrons. A search of the kSZ anisotropies due to the WHIM found no statistically significant evidence in *WMAP* data (Génova-Santos et al 2009). Only recently, Hernández-Montegudo et al (2015) and Planck Collaboration (2016) have presented evidence of the peculiar motion of extended gas on Mpc scales with a statistical significance at the $3 - 3.7\sigma$ level. Hill et al (2016) measured the kSZ effect correlating *WMAP* and *Planck* data with a galaxy sample from the Wide-field Infrared Survey Explorer (WISE)

¹ Física Teórica, Universidad de Salamanca, 37008 Salamanca, Spain; atrio@usal.es² Leibniz-Institut für Astrophysik, 14482 Potsdam, Germany; jp.muc@web.de

verifying that baryons approximately trace the Dark Matter (DM) distribution down to $\sim \text{Mpc}$ scales.

The cross-correlation of gravitational lensing maps with tSZ anisotropies is another potential probe of the relation between the hot, ionized gas and the matter density field. Hill & Spergel (2014) determined the cross-power spectrum of weak lensing of the CMB with the tSZ anisotropies measured by *Planck* at the 6σ confidence level, obtaining a constrain on the bias between the hydrostatic mass and the true mass of clusters and groups at redshifts $z \leq 2.5$. This authors interpreted their signal as being produced by baryons in halos. In parallel, Van Waerbeke, Hinshaw & Murray (2014) found a detection of the cross-correlation between the tSZ signal from *Planck* and the galaxy lensing convergence from the Canada-France-Hawaii Telescope Lensing Survey (CFHTLenS) with the same level of significance. Originally, the data were interpreted as the signal from warm and diffuse baryons. Since the distribution of galaxies in the survey peaks at $z = 0.37$, this result suggested that a large fraction of the missing baryon population had been identified. New studies and numerical simulations demonstrated that the majority of the signal came from a small fraction of baryons within halos (Ma et al 2015, Hojjati et al 2015, Battaglia, Hill & Murray, 2015). On large angular scales the simulations showed a correlation slightly above that of the halo model prediction, pointing to a 10 – 15% contribution from unbound gas. The latter contribution is degenerate with respect to cosmological and physical parameters and the data did not permit a robust inference (Battaglia et al 2015). Hojjati et al (2016) improved the statistical significance of the lensing – tSZ cross-correlation by using a larger weak lensing map derived from the Red Sequence Cluster Lensing Survey (RCSLenS) and found that their signal was best interpreted if AGN feedback removed a large quantity of hot gas from galaxy groups.

To estimate the contribution of unbound gas to the tSZ–lensing cross-correlation results described above requires an analytical model that correctly predicts the amplitude and shape of the expected signal. In Atrio-Barandela & Mückel (2006) we described the unbound gas in the weakly non-linear filaments by means of the log-normal Probability Distribution Function (PDF). In this article we use this description of the unbound gas to predict the cross-correlation of the lensing convergence due to the large scale matter distribution and the tSZ temperature anisotropies. The outline of this paper is as follows: In Section 2 we describe the model and compute the tSZ–convergence cross-correlation; the derived expressions are solved numerically and the results are presented in Section 3; finally, our conclusions are summarized in Section 4.

2. LENSING-TSZ CORRELATION IN THE FILAMENT MODEL.

The WHIM generates temperature anisotropies on the CMB via the tSZ. If n_e and T_e are the electron density and temperature along the line of sight then the anisotropy generated by the free electrons residing in the potential wells of the WHIM filaments in units of the current CMB black-body temperature T_0 is $\Delta T_{tSZ}/T_0 = Y_C G(\nu)$. The comptonization parameter measures the integrated electron pressure along the line of sight, $Y_C = k_B \sigma_T / m_e c^2 \int n_e T_e a dw$ with a the scale factor, w the comoving radial distance, $m_e c^2$ the electron annihilation temperature, k_B the Boltzmann constant and σ_T the Thomson cross section; $G(\nu) = (x \coth(x/2) - 4)$ gives the frequency dependence of the tSZ effect being $x = h\nu/k_B T_0$ the reduced frequency with h the Planck constant and ν the frequency of observation. This frequency dependence is different from that of any other known foreground making the tSZ anisotropy possible to distinguish from other CMB anisotropies given sufficient multi-frequency coverage. The data are usually expressed in terms of the comptonization parameter Y_C instead of the temperature anisotropy.

The intrinsic CMB temperature anisotropies are lensed by the large scale structure traced by galaxy catalogs. The tSZ anisotropies are themselves generated by the ionized gas within the same large scale structure. The two-point correlation function of the lenses and the spatial variations of the electron pressure along the line of sight is the weighted average of the lensing kernel $\Delta \kappa_{eff}$ due to the large scale structure traced by galaxy catalogs and the anisotropies generated by the tSZ effect of the ionized gas. The weight is given by the probability that the gravitational fields that lens the primary CMB anisotropies contain the electrons that generate the tSZ anisotropies. If the ionized gas generates a comptonization parameter $\Delta Y_C = (k_B \sigma_T / m_e c^2) n_e T_e a(dw/dz) dz$ at redshift z_1 in the direction \hat{x}_1 and the lenses are located at z_2 in direction \hat{x}_2 then their correlation is

$$C(\theta) \equiv \langle \kappa_{eff} Y_C \rangle(\theta) = \int_0^{z_H} \int_0^{z_H} \langle \Delta Y_C(\hat{x}_1, w_1) \Delta \kappa_{eff}(\hat{x}_2, w_2) \rangle dz_1 dz_2, \quad (1)$$

where θ is the angle between the directions \hat{x}_1 and \hat{x}_2 , i.e., $\cos \theta = \hat{x}_1 \cdot \hat{x}_2$ and w_1, w_2 are the comoving radial distances (for notation and definitions, see Bartelmann & Schneider 2001). The integration extends out to the redshift of the surface of the last scattering, z_H . The average $\langle \dots \rangle$ takes into account the distribution of the WHIM filaments and of the lenses and their correlation. Let us briefly summarize our WHIM model and the effect of a population of lenses before discussing their statistics.

2.1. The log-normal distribution of WHIM filaments.

Numerical simulations have shown that at redshifts $z > 1$ and at small scales the IGM forms filaments of mildly non-linear overdensities, giving rise to the observed Ly α forest. At $z < 1$ most of the IGM baryons resides in shock-heated regions of low density gas at temperatures 0.01 – 1KeV (Shull et al 2012) and sizes larger than 1 Mpc (Cen & Ostriker, 2006). We model the distribution of this unbound IGM gas as a log-normal random field evolving with time. The log-normal PDF was introduced in Cosmology by Coles & Jones (1991) to describe the non-linear distribution of matter in the Universe when the peculiar velocity field was still in the linear regime. Based on the improved Wiener density reconstruction from the Sloan Digital Sky Survey, Kitaura et al (2009) found that this distribution describes

the statistics of the matter inhomogeneities on scales larger than $7h^{-1}\text{Mpc}$. In the log-normal approximation, the number density of baryons at \vec{x} , located at redshift z and at a proper distance $|\vec{x}(z)|$ is $n_B(\vec{x}, z) = n_0(z)\xi$, where ξ is a log-normal distributed random variable normalized to have unit mean, $\langle \xi \rangle = 1$, and $n_0(z) = f_e \rho_B (1+z)^3 / \mu_B m_p$ is the mean baryon number density, ρ_B the baryon density, f_e the fraction of baryons in the WHIM, m_p the proton mass, $\mu_B = 4/(8-5Y)$ the mean molecular weight of the IGM and Y the He fraction by weight that we fixed to the value $Y = 0.24$. The non-linear baryon density contrast ξ in units of the baryon mean density should not be confused with δ or δ_B , respectively the matter and IGM baryon overdensities in the *linear regime*; ξ is given in terms of the gaussian distributed variable δ_B (Choudhury et al 2001, Atrio-Barandela & Mückel 2006)

$$\xi = e^{\delta_B(\vec{x}, z) - \sigma_B^2(z)/2}, \quad (2)$$

where $\sigma_B^2(z) = \langle \delta_B^2(\vec{x}, z) \rangle$ is the variance of the zero-mean linear IGM baryon density field. The number density of electrons in the IGM, n_e , is obtained by assuming equilibrium between recombination and photo-ionization and collisional ionization. For the conditions of the IGM, temperatures in the range $10^5 - 10^7\text{K}$ and density contrasts $\xi \leq 100$, the gas can be considered fully ionized so $n_e \approx n_B$.

The spectrum of density fluctuations of the baryons in the IGM is related to the DM density contrast δ_{DM} by (Fang et al 1993)

$$\delta_B(k, z) = \frac{\delta_{DM}(k, z)}{[1 + k^2 L_0^2]}. \quad (3)$$

The cut-off length L_0 corresponds to the scale below which baryon density perturbations are smoothed due to physical processes. The variance of the baryon density field is given by

$$\sigma_B^2(z) = \frac{D_+^2(z)}{2\pi^2} \int \frac{P_{DM}(k)}{[1 + L_0^2(z)k^2]^2} k^2 dk, \quad (4)$$

being $D_+(z)$ the linear growth factor of matter density perturbations.

2.1.1. Baryon damping scales.

At redshifts $z \leq 1$ small scale baryon perturbations are erased by shock-heating (Klar & Mückel 2010). If T_{IGM} is the mean IGM temperature, the comoving cut-off scale L_0 is determined by the condition that the linear velocity perturbation $\vec{v}(\vec{x}, z)$ averaged on a scale L_0 is equal to or larger than the IGM sound speed $c_s = (k_B T_{IGM}(z)/m_p)^{1/2}$. The IGM temperature is determined by the evolution of the UV background. At redshifts $z \leq 3$, the temperature varies within the range $T_{IGM} = [10^{3.6} - 10^4]\text{K}$ and its weakly dependent on redshift (Tittley & Meiksin, 2007). For $T_{IGM} = 10^4\text{K}$ the sound speed is $c_s \simeq 10\text{km/s}$; in our subsequent analyses we will fix the sound speed to this value at all redshifts. In the linear regime and in comoving coordinates, $\dot{\delta} = -(1+z)\nabla \vec{v}$ and $\dot{\delta} = Hf\delta$ with $f(z) = d \ln \delta / d \ln a$. In Fourier space, the peculiar velocity $\vec{v}(k)$ on a scale $k = 2\pi/L_0$ is $|\vec{v}(k, z)| \sim (L_0/2\pi)Hf(z)\delta(k, z)$. From the condition $|\vec{v}| \geq c_s$ and expressing $\delta(k, z) = \delta_0(k)D_+(z)$, with $\delta_0(k)$ the current amplitude of the density contrast at wavenumber $k = 2\pi/L_0$, we obtain $L_0 \geq [2\pi c_s](1+z)/[Hf(z)\delta_0(k)D_+(z)]$. This condition is valid only in the linear regime, hence the lower bound is obtained by imposing $\delta_0 \simeq 1$. Finally

$$L_0(z) = \frac{2\pi(1+z)c_s H_0^{-1}}{(\Omega_\Lambda + \Omega_m(1+z)^3)^{1/2} f(z) D_+(z)}, \quad (5)$$

where H_0 is the Hubble constant and Ω_Λ , Ω_m are the energy density of the cosmological constant and matter density in units of the critical density. In our numerical estimates, we fixed Ω_m , Ω_Λ to their concordance values. At $z = 0$ the comoving damping scale is $L_0 \approx 1.7h^{-1}\text{Mpc}$.

At redshifts $z \geq 1.0$, shock heating is no longer so effective and the damping scale L_0 corresponds to the comoving Jeans length at the conditions of the photo-ionized IGM

$$L_0(z) = H_0^{-1} \left[\frac{2\gamma k_B T_b(z)}{3\mu m_p \Omega_m(1+z)} \right]^{1/2}, \quad (6)$$

where γ the polytropic index and T_b the averaged background temperature of the IGM. This last parameter is little constrained by observations; Schaye et al (2000) argues that at $z \simeq 3$ HeII re-ionization requires T_b to be larger than $5 \times 10^4\text{K}$ while Viel & Haehnelt (2006) gave an upper bound of $T \simeq 2 \times 10^5\text{K}$. To simplify, we fix the average background temperature to the constant value $T_b = 10^5\text{K}$, within the interval allowed by observations.

2.1.2. The IGM temperature.

To describe the IGM distribution at all redshifts we will consider two limiting cases: At $z > 1$ the cut-off scale is the Jeans length given by eq. (6) and at $z \leq 1$ the shock-heated scale L_0 of eq. (5). To compute the tSZ contribution to CMB temperature anisotropies due to the IGM, we need to specify its temperature at each position and redshift. For the Jeans cut-off length scale we assume the temperature follows a polytropic equation of state $T(\hat{x}, z) = T_0(z)\xi^{(\gamma-1)}$. We take $T_0(z) = 1.4 \times 10^4(1+z)^\beta\text{K}$ in agreement with the values obtained by Hui & Haiman (2003), with a weak dependence

on redshift ($\beta \approx 0$). We chose $\gamma = 1.5$ and $\beta = 1$ as a conservative upper limit to WHIM tSZ anisotropies at $z \geq 1$. At $z \leq 1$, the shock heated IGM has a complex distribution of densities and temperatures. Kang et al (2005), hereafter K05, computes phase-space diagrams that can be fitted by the following equation of state: $\log_{10}(T_e(\xi)/10^8 K) = -2/\log_{10}(4 + \xi^{\alpha+1/\xi})$, valid for overdensities $\xi \leq 100$. Alternatively, Cen & Ostriker (2006), hereafter C06, find lower IGM temperatures; their phase-space diagram approximately corresponds to the equation of state $\log_{10}(T_e(\xi)/10^8 K) = -2.5/\log_{10}(4.0 + \xi^{0.9})$. We have considered all equations of state to be independent of redshift except the polytropic one. These models are represented in Fig. 1a; solid (black), dashed (blue) and dot-dashed (red) lines correspond to K05 with $\alpha = (3, 1.5, 1)$, respectively. The triple-dot dashed (green) line corresponds to C06 and the dotted (gold) line corresponds to the polytropic model at $z = 1$.

The overall amplitude of the cross-correlation function is proportional to the fraction of baryons in the WHIM and of the mean temperature of the electron gas. In our numerical estimates we have assumed that this baryon fraction is the same at all redshifts and equal to $f_e = 0.5$. The overdensity weighted temperature average $\bar{T}_e \equiv \langle T_e \xi \rangle / \langle \xi \rangle$ depends on the temperature model. For the K05 and C06 models this average in the interval overdensity $\xi = [1, 100]$ is $\bar{T}_e \approx [20, 7, 3, 0.7] \times 10^6 K$, weakly dependent on redshift; for the polytropic model, whose equation of state varies with redshift, the mean temperature is in the range $\bar{T}_e = [0.4 - 1.7] \times 10^6 K$. Any constrain on the amplitude of the cross-correlation will translate into an upper limit on the the product $f_e \bar{T}_e$ and if f_e is independently measured, then it would be a constrain on the mean temperature of the IGM, offering a direct probe onto the physical state of the WHIM.

2.2. Lensing kernel

The gravitational field generated by weak density perturbations lenses the radiation propagating in the Universe. The deflection angle of the weakly deflected rays can be related to an effective surface-mass density κ_{eff} , known as convergence, closely related to the mass distribution (Bartelmann & Schneider 2001). The convergence due to a population of lenses distributed as $G(w)dw = p(z)dz$ along the line of sight is

$$\kappa_{eff}(\hat{x}) = \frac{3H_0^2 \Omega_m}{2c^2} \int_0^{w_H} W(w) f_K(w) \frac{\delta[f_K(w)\hat{x}, w]}{a(w)} dw, \quad (7)$$

where \hat{x} is the direction in the sky into which the light ray starts to propagate, $f_K(w)$ is the comoving angular diameter distance at w , δ the matter density contrast along the unperturbed light ray and c the speed of light. The kernel weights the relative contribution of lenses along the line of sight

$$W(w) \equiv \int_w^{w_H} dw' G(w') \frac{f_K(w' - w)}{f_K(w')}. \quad (8)$$

The redshift distribution of galaxies is modeled as $p(z) = A(z/z_0)^2 \exp[-(z/z_0)^{3/2}]$, where z_0 is the effective depth of the lens population, related to the mean redshift of the distribution as $z_m = 1.412z_0$ (Smail et al 1995); the normalization constant is fixed by setting $\int p(w)dw = 1$. The distribution of galaxies in the CFHTLenS peaks at $z = 0.37$ (van Waerbeke et al 2014) that corresponds to $z_0 = 0.3$. These lens distributions are represented in Fig. 1b; dashed (blue), dot-dashed (red) and triple dot-dashed (green) lines correspond to $z = 0.1, 0.3, 0.5$ respectively. The more recent analysis by Hojjati et al (2016) uses the deeper RCSLenS catalog that includes all galaxies with $mag_r > 18$. These authors provide a numerical fit of their lens distribution, plotted in Fig. 1b with a solid (black) line.

From eq. (7), the contribution from lenses on a thin shell of width dz at comoving distance $w = w(z)$ and direction \hat{x} is

$$\Delta \kappa_{eff} = \frac{3H_0^2 \Omega_m}{2c^2} W(z) f_K(z) \frac{\delta[f_K(z)\hat{x}, z]}{a(z)} \frac{dw}{dz} dz. \quad (9)$$

In Fig. 1c we plot the convergence of eq. (9) for $\delta(f_K(w)\hat{x}, w) = 1$ as a function of redshift for the four lens distributions given in Fig. 1b, with lines following the same conventions. The integration range of eq. (7) must extend up to the horizon w_H or up to a redshift z^{up} high enough to include the effect of all possible lenses. We took $z^{up} = 5$, and no significant differences were found when taking $z^{up} = 10$. This is expected since the lensing kernel drops exponentially following the distribution of the lensing sources (see Figs. 1b and 1c).

Eq. (9) was derived in the thin lens approximation and only terms linear in the density contrast were retained. Higher order terms contain products of the density field but while the density contrast could be large for a density perturbation crossed by a given ray, the average overdensity is $\delta \ll 1$ for most rays and higher order terms can be safely neglected (Bartelmann & Schneider 2001). Within this approximation the PDF of the lenses is that of the linear density field and, consequently, is well described by a gaussian distribution.

2.3. Lensing - TSZ cross-correlation

To compute the correlation function of lenses and WHIM sources of tSZ anisotropies given by eq. (1), the average $\langle \dots \rangle$ has to account for the probability distribution of the WHIM filaments and of the lenses. Let $dP(\xi, \delta) = F(\xi, \delta) d\xi d\delta$ be the probability that a filament with overdensity ξ is located at (\hat{x}_1, z_1) when an overdensity δ is at (\hat{x}_2, z_2) , with

$F(\xi, \delta)$ the associated PDF. Then, the average in eq. (1) can be written as

$$\langle \Delta Y_C(\hat{x}_1, z_1) \Delta \kappa_{eff}(\hat{x}_2, z_2) \rangle(\theta) = \int_0^{z_1^{up}} dz_1 \int_0^{z_2^{up}} dz_2 \int_1^{100} d\xi \int_{-\infty}^{\infty} d\delta \Delta Y_C(\hat{x}_1, z_1) \Delta \kappa_{eff}(\hat{x}_2, z_2) F(\xi, \delta), \quad (10)$$

with $\cos \theta = \hat{x}_1 \cdot \hat{x}_2$ and z_1^{up} and z_2^{up} the highest redshifts beyond which WHIM and lenses do not generate a significant cross-correlation. To complete our model we need to specify the bivariate PDF of the lens-filament distribution, $F(\xi, \delta)$. As discussed above, lensing is dominated by the large scale structure and the lensing overdensities δ are well described by a gaussian PDF, but the non-linear overdensities ξ of the IGM filaments are distributed according to a log-normal PDF. Since $\xi = Ae^{\delta_B}$ is log-normal distributed, $\log(\xi)$ follows a gaussian distribution with mean $\mu_\xi = -\sigma_B^2/2$ and variance σ_B^2 ; in term of this variable the probability can be written as $dP = \mathcal{G}(\log(\xi), \delta) d\log(\xi) d\delta$ where \mathcal{G} is a bivariate gaussian and

$$F(\xi, \delta) = \frac{1}{2\pi\xi\sigma_B\sigma_\delta(1-\rho_c)^{1/2}} \exp \left[\frac{1}{2(1-\rho_c^2)} \left(\frac{(\log \xi - \sigma_B^2/2)^2}{\sigma_B^2} - 2\rho_c \frac{(\log \xi - \sigma_B^2/2)(\delta - \mu_\delta)}{\sigma_B\sigma_\delta} + \frac{(\delta - \mu_\delta)^2}{\sigma_\delta^2} \right) \right]. \quad (11)$$

In this expression μ_δ is the mean of the matter density contrast, in this case $\mu_\delta = 0$. The variance of the matter density field is $\sigma_\delta^2 = (D_+^2(z)/2\pi^2) \int P_{DM}(k) k^2 dk$. At small scales, $P_{DM}(k) \propto k^{-3}$ and the integral is logarithmically divergent. Therefore, we remove small scale perturbations by filtering the density field with a *top-hat* window of radius $R_{cut} = 0.5h^{-1}\text{Mpc}$. Physically this corresponds to removing from the lensing kernel the contribution from galaxies, groups and clusters. Then

$$\sigma_\delta^2 = \frac{D_+^2(z)}{2\pi^2} \int P_{DM}(k) W_{th}^2(kR_{cut}) k^2 dk, \quad (12)$$

where $W_{th}(kR_{cut})$ is the Fourier transform of the *top-hat* filter. Changing the cut-off scale to $R_{cut} = 1h^{-1}\text{Mpc}$ reduces σ_δ by a factor 0.85. The coefficient $\rho_c = \langle \log \xi \delta \rangle / \sigma_B \sigma_\delta$ is the correlation between two gaussian variables

$$\rho_c(r) = \frac{D_+(z_1)D_+(z_2)}{2\pi^2\sigma_\xi\sigma_\delta} \int \frac{P_{DM}(k)}{1 + L_0^2(z_1)k^2} W_{th}(kR_{cut}) j_0(k|\vec{x}_1 - \vec{x}_2|) k^2 dk, \quad (13)$$

where j_0 is the 0th order spherical Bessel function and $r = |\vec{x}_1 - \vec{x}_2|$ is the comoving distance between a filament in the IGM at \vec{x}_1 and a lens at \vec{x}_2 , corresponding to redshifts z_1 and z_2 , and separated by an angle θ . As in Suarez-Velásquez, Mückel & Atrio-Barandela (2013a) we use the flat sky approximation and

$$r \equiv |\vec{x}_1 - \vec{x}_2| \approx \sqrt{l_\perp(\theta, z_1)^2 + [w(z_1) - w(z_2)]^2}, \quad (14)$$

with $l_\perp(\theta, z_1)$ being the transverse distance between two points located at the same redshift. Notice that $\rho_c(0) \neq 1$, since the two distributions, IGM and lenses, are not fully correlated.

In Fig. 1d we represent the absolute value of the correlation coefficient for different cosmological parameters. We assume a flat Universe, i.e., $\Omega_m + \Omega_\Lambda = 1$. The matter power spectrum is normalized to $\sigma_8 = 0.8$. We verified that varying parameters within the ranges given in Fig. 1d has an effect on the comptonization-convergence cross-correlation that is small compared with the differences in the lens distribution or the equation of the state of the IGM temperature, so we will not discuss further variations of cosmological parameters and their effect on our results.

3. RESULTS AND DISCUSSION.

We compute the comptonization-convergence cross-correlation using eq. (10). The integration over the lensing part extends up to the redshift of the last scattering surface. However, as Fig. 1c indicates, the lensing kernel drops exponentially following the distribution of the lensing sources and, effectively, we can stop the integration at $z_2^{up} = 1, 2.6, 4.6$ for lens distributions with $z_0 = 0.1, 0.3, 0.5$, respectively, when the kernel has decreased by a factor 10^{-15} from its maximum value. For RCSLenS sources the integration stops at $z_2^{up} = 4.6$ when similar drop factor has been reached. We verified that, as expected, extending the integration further does not increase the cross-correlation.

More delicate is to decide out to what redshift is valid our model of the IGM. At $z \geq 1$ shock-heating stops being dynamically important. In Fig. 2a we compute the amplitude of the effective lensing-comptonization cross-correlation at zero lag, $C(0) = \langle \kappa_{eff} Y_C \rangle(0)$ as a function of the upper limit of integration z_1^{up} . The results, from top to bottom correspond to the K05 with $\alpha = 3, 1.5, 1$ (black solid, dashed blue and dot-dashed red lines) and the C06 model (triple dot-dashed green line). In Fig. 2b we plot the differential contribution. This figure indicates that most of the cross-correlation originates from $z \leq 1$.

Since the cross-correlation scales with the fraction of electrons in the IGM as $\langle \kappa_{eff} Y_C \rangle \propto (f_e/0.5)$, we need to know the fraction of electrons in the WHIM to translate constraints on $C(0)$ into constraints in the mean temperature of the gas. Although 80% of all baryons reside in Ly α systems at redshift $z \simeq 2$ and $f_e \leq 0.2$ at that redshift (Fukugita et al 1998), numerical simulations indicate that $f_e \geq 0.4$ out to $z \simeq 1$ (C06), the range in redshift space that dominates the cross-correlation. Therefore, by taking $f_e = 0.5$ and constant our constraints on the mean WHIM temperature will be reasonably accurate.

The contribution of the IGM comptonization parameter to the cross-correlation from $z \geq 1$ is less than 10%. In fact, this correction is overestimated. First, the fraction of baryons in the WHIM drops with redshift. Second, and

as mentioned in Sec 2.1.2, the IGM behaves as a polytrope and, on average, its temperature is smaller than the K05 shock-heated models and is similar to C06 (see also Fig 1a). In the interval $z \geq 1$ the cross-correlation with the polytropic equation of state and the damping scale of eq. (6) is $\langle \kappa_{eff} Y_C \rangle \sim 1 - 10 \times 10^{-12}$ for the different lens distributions. This is a very small contribution and essentially we could have stopped our calculation at $z = 1$ or extend the shock model out to $z = 3$ since it would have introduced an error smaller than 10%. We adopted this latter option and by not including the Jeans cut-off scale (eq. 6) and its corresponding polytropic equation of state, we simplify the parameter space of our model and the physical interpretation of our results.

Figs. 3 and 4 constitute our main result. In Fig. 3 we plot the $\langle \kappa_{eff} Y_C \rangle$ cross-correlation for the three lens distributions with $z_0 = 0.1, 0.3, 0.5$ (upper panels) and their corresponding power spectra (lower panels). The power spectrum is computed from the correlation function integrating the quadrature

$$C_\ell = 2\pi \int \langle \kappa_{eff} Y_C \rangle P_\ell(\cos \theta) d \cos \theta, \quad (15)$$

with P_ℓ the ℓ -th Legendre polynomial. Hence, we are required to compute the correlation function over the range $\theta = [0, \pi]$ rad. To simplify our calculation we have assumed the sky to be flat (eq. 14) and although this approximation limits the accuracy of the low- ℓ multipoles, it should be accurate for multipoles where data is available, $\ell \geq 100$.

In the panels of Fig. 3 and from top to bottom the solid (black), dashed (blue) and dot-dashed (red) lines correspond to K05 with $\alpha = 3, 1.5, 1$ and the triple dot-dashed (green) line corresponds to C06. The distribution of the CFHTLenS is well approximated by $z_0 = 0.3$ then, in Fig. 3b we also plot the data from van Waerbeke et al (2014) and their respective error bars. In Fig. 4 we plot the correlation function and the power spectrum for the same shock-heating temperature models but for the RCSLenS sources with $mag_r > 18$. Lines follow the same conventions than in Fig. 3. The data are taken from Hojjati et al (2016).

To analyze the contribution of the different IGM overdensities we divide the integration of eq. (10) in four intervals with equal logarithmic spacing: $\xi = ([1 - 3.3], [3.3 - 10], [10 - 33], [33 - 100])$. We computed the contribution in each interval for the K05 with $\alpha = 1.5$ and for lens distributions $z_0 = 0.3$ (Fig. 3b) and RCSLenS sources (Fig. 4a). The fractional contribution to the correlation at the origin, $\langle \kappa Y_C \rangle(0)$, was (0.08, 0.45, 0.41, 0.06) for the first case and (0.1, 0.39, 0.46, 0.05) in the second. Similar results occur for other lens distributions and temperature models: most of the correlation comes from overdensities in the range $\xi \approx [3 - 33]$. The numerical simulations of Davé et al (2001) found that this is the density range where most of the WHIM is stored. In this respect, if our log-normal model were to be accurate only at these intermediate overdensities, integration of eq. (10) would still provide a very accurate result.

The comparison of the measured data with the theoretical predictions already offers some insights into the nature of the IGM. For the CFHTLenS sources shown in Fig 3b, all temperature models are allowed by the data. As indicated in Sec. 2.1.2, the shock-heating model with $\alpha = 3$ corresponds to an average temperature of $\bar{T}_e = 2 \times 10^7$ K and is still compatible with the measured correlation. However, our results do not include the contribution due to clusters and galaxy groups. Since at most 15% of the measured signal comes from unbound gas if we restrict the overall IGM contribution to be that fraction of the overall signal then only models with $\alpha \leq 1.5$ are compatible with the data. In other words, the mean temperature of the IGM free electron gas would be $\bar{T}_e \leq 7 \times 10^6$ K.

The data from Hojjati et al (2016) shown in Fig 4a are even more restrictive. These authors compared their measurements against the predictions of the halo model and from numerical simulations that included diffuse gas. The simulations showed a very good agreement with the observed cross-correlation from RCSLenS galaxies, with about 10-15% contributions coming from unbound gas. The amplitude of the correlation (Fig 4a) in the range $\theta = [40 - 120]$ arcmin is that of the $\alpha = 1.5$ model. In that interval, only the C06 temperature model predicts an amplitude 10% of the measured correlation. That would imply that the average temperature of the IGM is $\bar{T}_e \sim 10^6$ K, a stricter bound than derived from the van Waerbeke et al (2014) data.

There is a caveat when translating the results on the cross-correlation onto an upper limit on the average temperature of the IGM. Hydro-simulations consistently show that unbound gas is not well characterized by a single equation of state; more accurately, the gas coexists in different phases and there is a large spread in temperature within regions with the same overdensity. Since our temperature models fails to encode the full complexity of the temperature-density phase diagram, our upper bounds on the average temperature must be understood as an order of magnitude estimate not as a strict upper limit.

The constraints that can be derived from the measured power spectrum shown in Fig. 4b are not as tight as those derived from the correlation function. Only the measurement at $\ell \sim 1800$ is well below the prediction for the K05 models. What is more relevant is that the overall shape is very different. Hojjati et al (2016) found that the shape of the correlation function and power spectrum was strongly dependent on physical processes undergone by baryons in halos such as radiative cooling, star formation, supernovae winds and AGN feedback. For instance, AGNs expel gas to large distances from the center of halos, lowering the signal at small scales. The properties of the hot gas in our model are rather simplified. No effects of specific physical processes are considered and only the density and temperature distributions are important. More realistic models would require detailed numerical simulations including the most relevant processes in low density regions. Physical effects could remove power at $\ell \geq 1000$, modifying the overall shape of the power spectrum and bringing it in closer agreement with the data. While a detailed discussion on this point is beyond the scope of the current paper, if the shape were to be independent of the physics of baryons the power spectrum could be a useful discriminant between halo and unbound gas contributions.

An alternative approach to detect the WHIM contribution would be to remove known galaxies down to a given

magnitude to eliminate the contribution of their halos to the comptonization-convergence correlation. When removing fainter galaxies does not produce a further decrement of the cross-correlation, we have reached the level when the signal is due to gas outside halos. A similar approach has been used by Kashlinsky et al (2005) and Helgason et al (2015) to isolate Cosmic Infrared Background fluctuations due to first stars at the epoch of reionization from those of known galaxy populations in deep Spitzer data.

4. CONCLUSIONS.

Models of galaxy formation predict that a significant fraction, close to half the total number of baryons, could be stored in the WHIM. The low densities and temperatures $10^5\text{--}10^7\text{K}$ of this medium makes it difficult to detect. Search for absorption lines and SZ contributions have provided preliminary evidence of its existence. The $\langle\kappa Y_C\rangle$ cross-correlation measured by Van Waerbeke et al (2014) and Hojjati et al (2016) probes the fluctuations on the electron pressure along the line of sight and its distribution but it is not yet a detection of the missing baryon component. As indicated by Hojjati et al (2015) about 50% of the signal comes from the small fraction of baryons within massive halos; at most, 15% of the cross-correlation power at $\ell \sim 500$ could come from unbound gas. In this article we have shown that the contribution from the unbound gas in filaments could be of this order of magnitude, depending on model parameters. In particular, if the unbound gas is well described by a log-normal distribution and the gas is shock heated out to a mean temperature $\bar{T}_e \sim 10^6\text{K}$, then about half the baryons on the Universe could be stored in the WHIM producing a signal that is at least one order of magnitude smaller than the measured amplitude. We have considered two different baryon cut-off lengths: the Jeans length given by eq. (6) that would describe better the physical state of the IGM at $z > 1$ and the shock-heated cut-off scale given by eq. (5), that provides a better description at $z < 1$. We have shown that $\sim 90\%$ of the contribution to the $\kappa_{eff} - Y_C$ cross-correlation and to its power spectrum originates at $z \leq 1$ and at overdensities in the range $\xi \sim [3 - 33]$. The overall amplitude depends on the depth of the source catalog probing the convergence due to the large scale structure, the average electron temperature and is proportional to the fraction of baryons in the IGM.

The tSZ-lensing cross-correlation could be a potentially powerful technique to trace the distribution of baryons at large scales. The shape of the measured comptonization-convergence power spectrum and the theoretical prediction for IGM gas show maxima at different scale. The difference could be due to not having include the physical effects that are relevant to the evolution of the IGM gas; but if the differences in shape are real, they could be used to separate the contribution of unbound gas from that of gas in halos. In real space, the cross-correlation is also dominated by halos. To detect the contribution due to the WHIM would require to mask galaxy populations with increasing magnitude down to the level when further masking does not reduce the residual correlation. This would require to extend the measurement to larger areas and to deeper lens surveys, as Hojjati et al (2016), to increase the signal-to-noise by a factor 5-10. Then, masking the halo contribution down to 10% of its original amplitude would still leave a statistically significant signal.

Acknowledgments

F. A.-B. acknowledges financial support from the grant FIS2015-65140-P (MINECO/FEDER). He also thanks the hospitality of the Leibniz Institute für Astrophysik at Potsdam where part of this work was done.

REFERENCES

- Atrio-Barandela, F., Kashlinsky, A., Ebeling, H., Fixsen, D. J., Kocevski, D. 2015, *ApJ*, 810, 143
- Atrio-Barandela, F., & Mückel, J. P. 2006, *ApJ*, 643, 1
- Atrio-Barandela, F., Mückel, J. P. & Génova-Santos, R., 2008, *ApJL*, 674, L61
- Bartelmann, M. & Schneider, P., 2001, *Phys. Rep.*, 340, 291
- Battaglia, N., Hill, J. C. & Murray, N. 2015, *ApJ*, 812, 154
- Cappelluti N., Ranalli, P., Roncarelli, M., Arevalo, P., Zamorani, G., Comastri, A., Gilli, R., Rovilos, E., Vignali, C., Allevato, V., Finoguenov, A., Miyajii, T., Nicastro, F., Georgantopoulos, I. & Kashlinsky, A., 2012, *MNRAS*, 247, 651
- Cen, R., & Ostriker, J. P. 1999, *ApJL*, 519, L109
- Cen, R., & Ostriker, J. P. 2006, *ApJ*, 650, 560 (C06)
- Choudhury, T. R., Padmanabhan, T. & Srianad, R. 2001, *MNRAS*, 322, 561
- Coles, P., & Jones, B. J. T. 1991, *MNRAS*, 248, 1
- Davé, R., Cen, R., Ostriker, J. P., Bryan, G. L., Hernquist, L., Katz, N., Weinberg, D. H., Norman, M. L. & O’Shea, B. 2001, *ApJ*, 552, 473
- Davé R., Hernquist, L., Katz, N. & Weinberg, D. H. 1999, *ApJ*, 511, 521
- De Bernardis, F., Aiola, S., Vavagiakis, E. M. et al. 2017, *JCAP*, 03, 008
- Eckert, D., Jauzac, M., Shan, H. Y., Kneib, J.-P., Erben, T., Israel, H., Jullo, E., Klein, M. et al, 2015, *Nature*, 528, 105
- Fang, L. Z., Bi, H., Xiang, S., & Börner, G. 1993, *ApJ*, 413, 477
- Fukugita, M., Hogan, C. J., & Peebles, P. J. E. 1998, *ApJ*, 503, 518
- Génova-Santos, R., Atrio-Barandela, F., Mückel, J. P., & Klar, J. S. 2009, *ApJ*, 700, 447
- Génova-Santos, R., Suarez-Velázquez, I., Atrio-Barandela, F. & Mückel, J. P., 2013, *MNRAS*, 432, 2480
- Génova-Santos, R., Atrio-Barandela, F., Kitaura, F.-S. & Mückel, J. P., 2015, *ApJ*, 806, 113
- Hand, N., Addison, G. E., Aubourg, E. et al. 2012, *Phys. Rev. Lett.* 109, 041101
- Helgason, K., Ricotti, M., & Kashlinsky, A. 2012, *ApJ*, 752, 113
- Hernández-Monteagudo, C, Ma, Y-Z, Kitaura, F. S., Wang, W, Génova-Santos, R, Macías-Pérez & J. Herranz, D. 2015, *PRL*, 115, 191301
- Hill, J.C., Ferraro, S., Battaglia, N., Liu, J. & Spergel, D. N. 2016, *PRL*, 117, 1301
- Hill, J.C. & Spergel, D. N. 2014, *JCAP*, 2, 30
- Hojjati, A., McCarthy, I. G., Harnois-Déraps, J., Ma, Y.-Z., Van Waerbeke, L., Hinshaw, G. & Le Brun, A. M. C. 2015, *JCAP*, 10, 047
- Hojjati, A., Tröster, T., Harnois-Déraps, J., McCarthy, I. G., Van Waerbeke, L., Choi, A. et al. 2016, *ArXiv1608.07581*
- Hui, L., & Haiman, Z. 2003, *ApJ*, 596, 9
- Kang, H., Ryu, D., Cen, R. & Song, D. 2005, *ApJ*, 620, 21(K05)
- Kashlinsky, A., Arendt, R. G., Mather, J., & Moseley, S. H. 2005, *Nature*, 438, 45

- Kashlinsky, A., Atrio-Barandela, F., Kocevski, D., Ebeling, H. 2008, *ApJL*, 686, L49
- Klar, J. S. & Mücke, J. P. 2010, *A&A*, 522, 114
- Kitaura, F. S., Jasche, J., Li, C., et al. 2009, *MNRAS*, 400, 183
- Lehner, H., Savage, B. D., Richter, P. et al 2007, *ApJ*, 658, 680
- Ma, Y.-Z., Van Waerbeke, L., Hinshaw, G., Hojjati, A., Scott, D., Zuntz, J. 2015, *JCAP*, 9, 046
- McQuinn, M. 2016, *ARAA*, 54, 313
- Penton, S. V., Stocke, J. T. & Shull, J. M. 2004, *ApJS*, 152, 29
- Planck Collaboration. Planck Intermediate Results VIII. Filaments between interacting clusters, 2013, *A&A*, 550, A134
- Planck Collaboration. Planck Intermediate Results CV. Evidence of unbound gas from the kinetic Sunyaev-Zeldovich effect, 2016, *A & A*, 586, A140
- Roncarelli M., Cappelluti N., Borgani S., Branchini E., Moscardini L., 2012, *MNRAS*, 424, 1012
- Schaan, E., Ferraro, S., Vargas-Magaña, M. et al. 2016 *Phys. Rev. D* 93, 082002
- Schaye, J., Theuns, T., Rauch, M., Efstathiou, G., & Sargent, W. L. W. 2000, *MNRAS*, 318, 817
- Soergel, B., Flender, S., Story, K. T. et al. 2016 *MNRAS*, 461, 3172
- Soltan, A. M. 2006, *A&A*, 460, 59
- Shull, J. M., Smith, B. D., & Danforth, D. W. 2012, *ApJ*, 759, 23
- Smail, I., Hogg, D. W., Yan, L. & Cohen, J. G. 1995, *ApJ*, 449, L105
- Smith, B. D., Hallman, E., Shull, J. M., & OShea, B. 2011, *ApJ*, 731, 6
- Suarez-Velázquez, I. F., Mücke, J. P., & Atrio-Barandela, F. 2013a, *MNRAS*, 431, 342
- Suarez-Velázquez, I. F., Kitaura, F. S., Atrio-Barandela, F. & Mücke, J. P. 2013b, *ApJ*, 769, 25
- Sunyaev, R. A., & Zel'dovich, Y. B. 1970, *ApSS*, 7, 3
- Sunyaev, R. A., & Zel'dovich, Y. B. 1972, *CoASP*, 4, 173
- Tittley, E. & Meiksin, A. 2007, *MNRAS*, 380, 1369
- Ursino, E., Galeazzi, M. & Hufferberger, K. 2014, *ApJ*, 789, 55
- Van Waerbeke, L., Hinshaw, G. & Murray, N. 2014, *Phys Rev D*, 89, 023508
- Viel, M., & Haehnelt, M. G. 2006, *MNRAS*, 365, 231

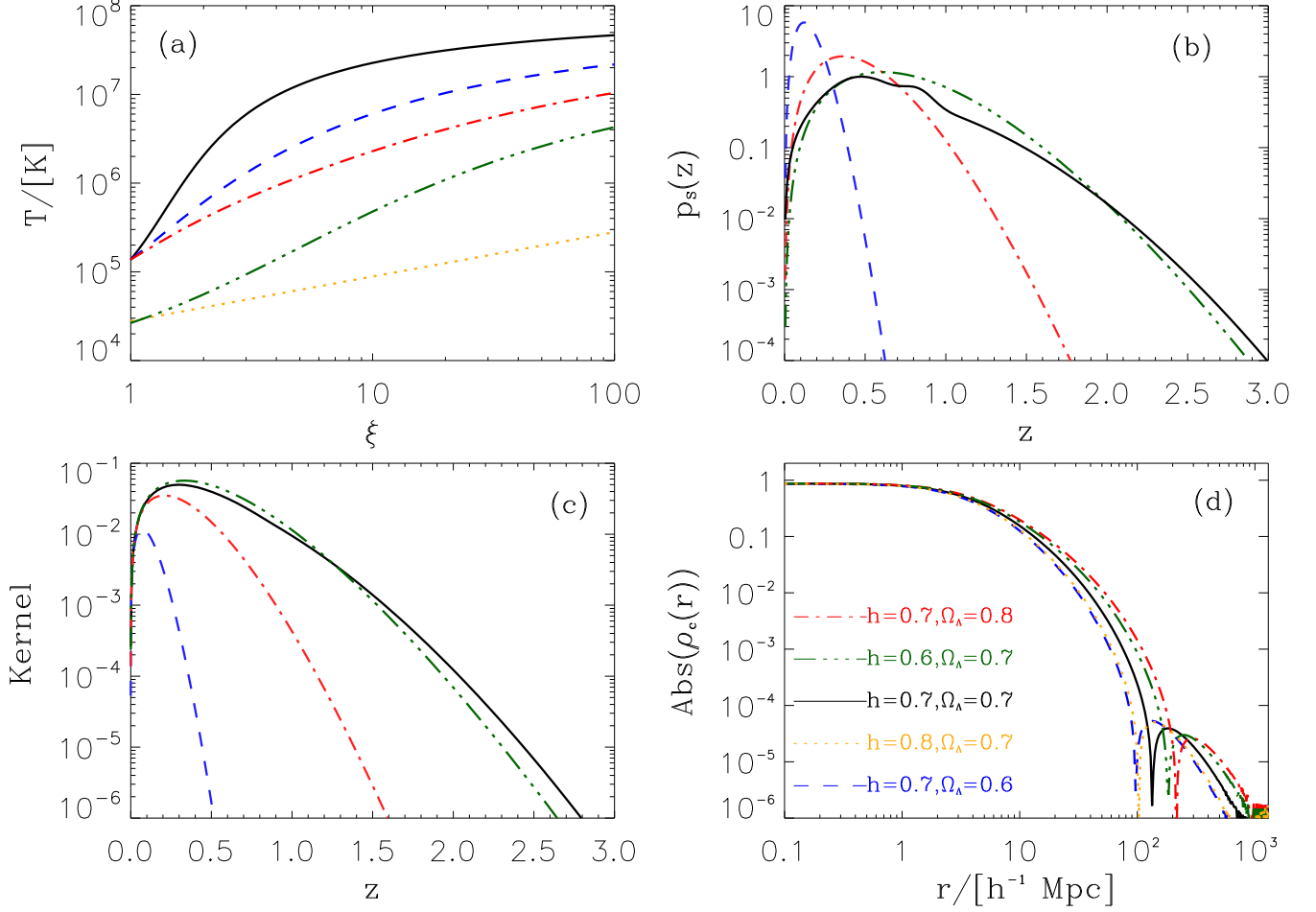


FIG. 1.— (a) IGM temperature models considered in this paper; solid (black), dashed (blue) and dot-dashed (red) lines correspond to K05 with $\alpha = (3, 1.5, 1)$, the triple-dot dashed (green) line corresponds to C06 and the dotted (gold) line to the polytropic model at $z = 1$, respectively. (b) Distribution of the lensing sources for $z_0 = 0.1$ (dashed blue), $z_0 = 0.3$ (solid blue) and $z_0 = 0.5$ (dot-dashed blue). For comparison, the thick solid black line shows the distribution of the RCSLenS sources with $mag_r > 18$. (c) Lensing kernel for the four distributions of the lensing sources. Lines follow the same conventions as in (b). (d) Correlation coefficient of eq. (13) for different cosmological parameters.

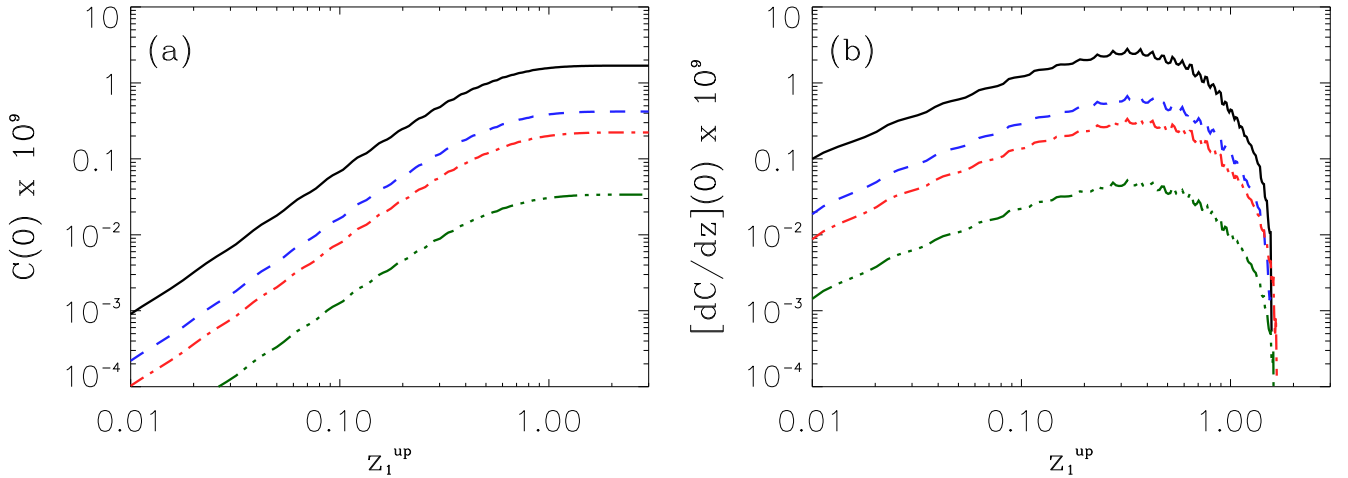


FIG. 2.— Amplitude of the convergence-comptonization cross-correlation at the origin, $C(0) = \langle \kappa_{eff} Y_C \rangle(0)$ as a function of the upper limit of integration z_1^{up} . The results, from top to bottom correspond to K05 with $\alpha = 3, 1.5, 1$ (black solid, dashed blue and dot-dashed red lines) and C06 (triple dot-dashed line). The lens distribution is the numerical fit to the RCSLenS sources. The baryon cut-off scale is given by eq. (5).

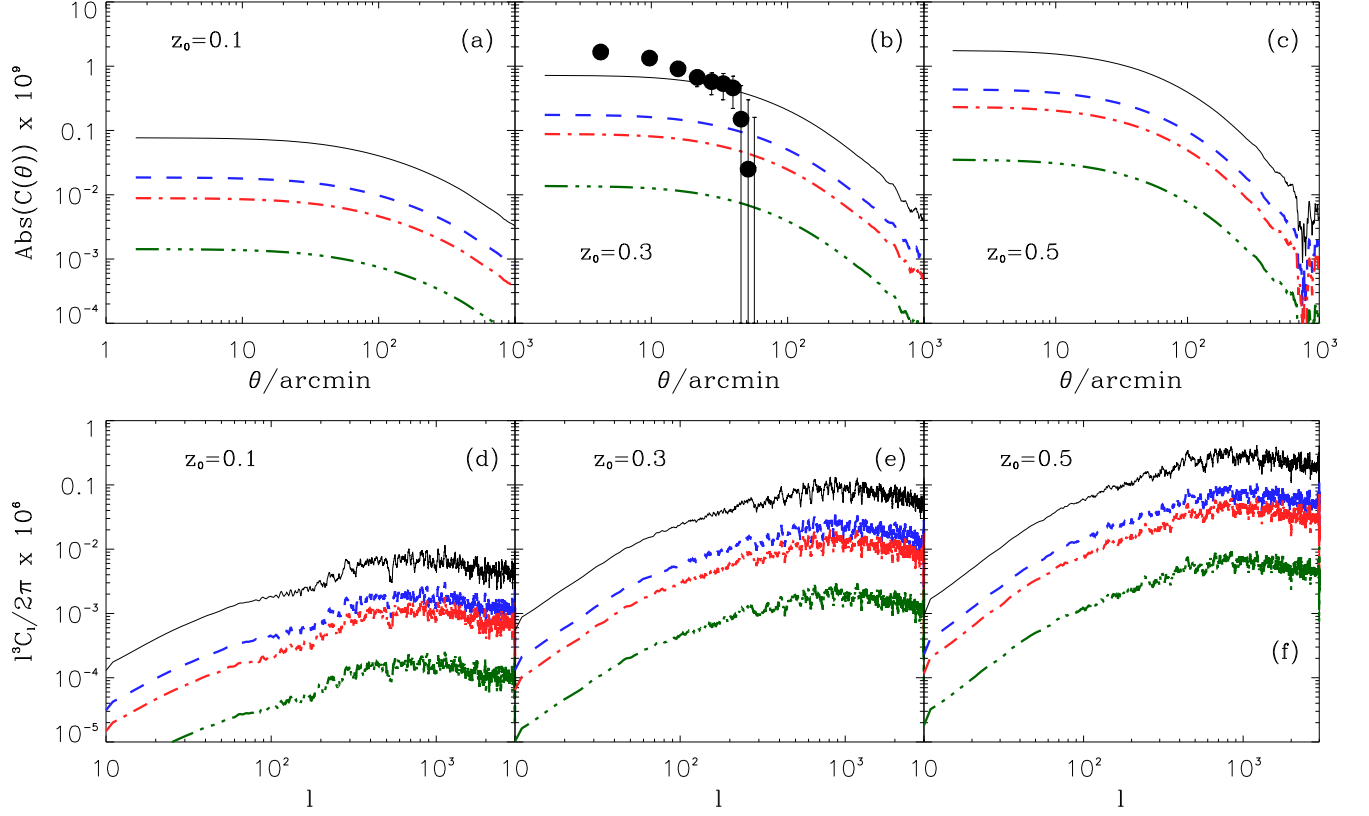


FIG. 3.— Comptonization parameter-lensing convergence cross-correlation (upper panels) and power spectrum (lower panels) for lens source catalogs of different scale z_0 . The cut-off scale is given by eq. (5). From top to bottom, lines correspond to K05 with $\alpha = 3, 1.5, 1$ (solid black, dashed blue and dot-dashed red, respectively) and C06 (triple dot-dashed line). The corresponding power spectra are shown in the bottom panels with line following the same conventions. In (b) the correlation data and error bars were taken from Van Waerbeke et al (2014).

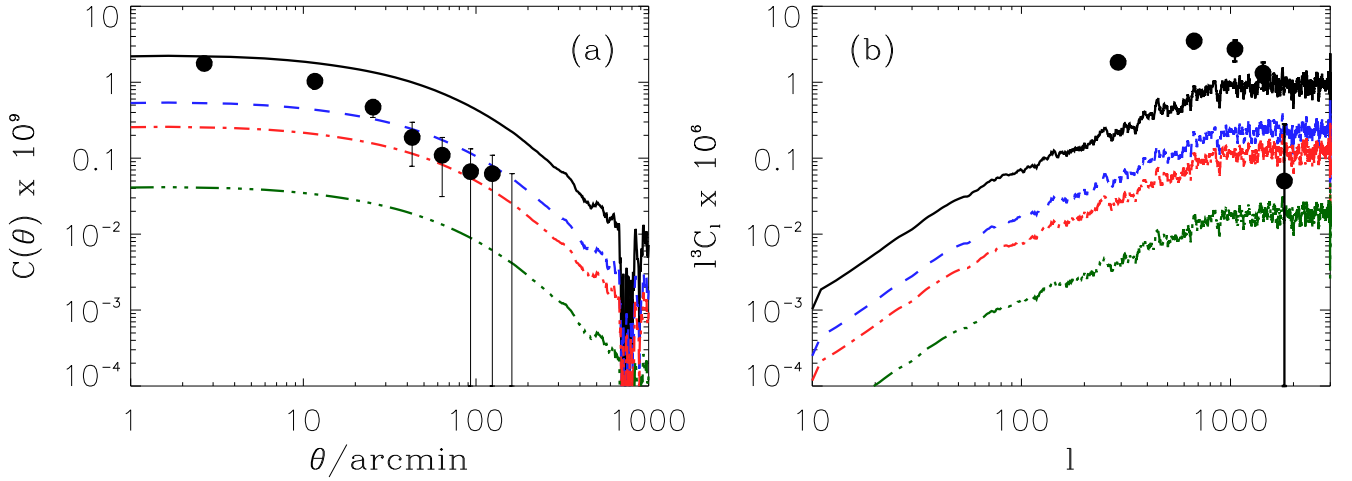


FIG. 4.— Comptonization-convergence correlation and power spectrum due to the RCSLenS sources with $mag_r > 18$. Lines follow the same conventions as in Fig. 3. The correlation and power spectrum data points were taken from Hojjati et al (2016).